



Full length article

## A lightweight, biological structure with tailored stiffness: The feather vane



Tarah N. Sullivan<sup>a,b</sup>, Andrei Pissarenko<sup>b</sup>, Steven A. Herrera<sup>c</sup>, David Kisailus<sup>c</sup>, Vlado A. Lubarda<sup>a,b,d</sup>,  
Marc A. Meyers<sup>a,b,d,\*</sup>

<sup>a</sup> Materials Science and Engineering Program, University of California, San Diego, La Jolla, CA 92093, USA

<sup>b</sup> Department of Mechanical and Aerospace Engineering, University of California, San Diego, La Jolla, CA 92093, USA

<sup>c</sup> Department of Chemical and Environmental Engineering, University of California, Riverside, Riverside, CA 92521, USA

<sup>d</sup> Department of Nano Engineering, University of California, San Diego, La Jolla, CA 92093, USA

### ARTICLE INFO

#### Article history:

Received 25 February 2016

Received in revised form 4 May 2016

Accepted 12 May 2016

Available online 13 May 2016

#### Keywords:

Biological hierarchical structure

Lightweight structure

Feather morphology

### ABSTRACT

The flying feathers of birds are keratinous appendages designed for maximum performance with a minimum weight penalty. Thus, their design contains ingenious combinations of components that optimize lift, stiffness, aerodynamics, and damage resistance. This design involves two main parts: a central shaft that prescribes stiffness and lateral vanes which allows for the capture of air. Within the feather vane, barbs branch from the shaft and barbules branch from barbs, forming a flat surface which ensures lift. Microhooks at the end of barbules hold barbs tightly together, providing the close-knit, unified structure of the feather vane and enabling a repair of the structure through the reattachment of un-hooked junctions. Both the shaft and barbs are lightweight biological structures constructed of keratin using the common motif of a solid shell and cellular interior. The cellular core increases the resistance to buckling with little added weight. Here we analyze the detailed structure of the feather barb and, for the first time, explain its flexural stiffness in terms of the mechanics of asymmetric foam-filled beams subjected to bending. The results are correlated and validated with finite element modeling. We compare the flexure of single barbs as well as arrays of barbs and find that the interlocking adherence of barbs to one another enables a more robust structure due to minimized barb rotation during deflection. Thus, the flexure behavior of the feather vane can be tailored by the adhesive hooking between barbs, creating a system that mitigates damage. A simplified three-dimensional physical model for this interlocking mechanism is constructed by additive manufacturing. The exceptional architecture of the feather vane will motivate the design of bioinspired structures with tailored and unique properties ranging from adhesives to aerospace materials.

#### Statement of Significance

Despite its importance to bird flight, literature characterizing the feather vane is extremely limited. The feather vane is composed of barbs that branch from the main shaft (rachis) and barbules that branch from barbs. In this study, the flexural behavior of the feather barb and the role of barbule connections in reinforcing the feather vane are quantitatively investigated for the first time, both experimentally and theoretically. Through the performed experiments, structure-function relationships within the feather vane are uncovered. Additionally, in the proposed model the sophisticated structure of the barbs and the interlocking mechanism of the feather vane are simplified to understand these processes in order to engineer new lightweight structures and adhesives.

© 2016 Acta Materialia Inc. Published by Elsevier Ltd. All rights reserved.

\* Corresponding author at: Materials Science and Engineering Program, University of California, San Diego, 9500 Gilman Drive, La Jolla, CA 92093, USA.

E-mail address: [mameyers@eng.ucsd.edu](mailto:mameyers@eng.ucsd.edu) (M.A. Meyers).

### 1. Introduction

The complex design of the modern feather evolved during the Late Jurassic period along with the advancement of aerial locomotion [1]. This unusual integument derived from less sophisticated

filaments used for sexual selection and (or) thermoregulation in dinosaurs [2,3]. Contemporary bird feathers, composed exclusively of  $\beta$ -keratinous material, are extremely specialized and diverse and range from bristles (analogous to whiskers in mammals) to downy feathers [4].

The flight feather consists of a main shaft (rachis and calamus, Fig. 1a), and a feather vane composed, sequentially, of barbs that branch from the rachis (Fig. 1b) and barbules that branch from barbs (Fig. 1c). Flight feathers must be lightweight and able to sustain aerodynamic loads without excessive flexure/torsion and damage. One of the ways feather components conform to these constraints is by having a sandwich structure, consisting of a solid shell and cellular core. Their dense exterior is composed of layers of ordered fibers in a matrix material which form a biological composite laminate on the micro-scale. According to a study by Lingham-Soliar et al. [5], both the barb and rachis have fibers oriented in the axial direction along dorsal and ventral sides with thin crossed-fibers in the lateral walls.

Within the feather vane, barbs form a highly ordered lattice where they interlock with adjacent barbs via barbules to produce a tightly woven structure. On a given barb, proximal barbules have a grooved structure while distal barbules have four to five tiny microhooks (hooklets) along their length (Fig. 1d) [6,7]. Hooked barbules interlock with the neighboring barb's grooved barbules to form a "Velcro-like" connection that can be separated and re-zipped [8]. This enables repair of the damaged areas by re-hooking the hooks to grooves.

The innovation of the interlocking feather vane is credited as the essential element which makes flight possible in birds [9,10] as it allows for a compact and cohesive structure for aerodynamic efficiency [11]. The air transmissivity of the feather is a function of how tightly connected barbs are, and birds preen themselves daily to re-zip their feather vanes [12]. Similarities in the barb structure and interlocking mechanism across bird species are

demonstrated in Fig. 2, where feathers of the razor-billed curassow (*Mitu tuberosum*), house sparrow (*Passer domesticus*), and California seagull (*Larus californicus*) are shown. Since these structures are similar in nearly all flying birds [6], structural deformation concepts can be generalized to apply to most feathers.

While barbules are an essential part of the feather vane, barbs make the greatest contribution to its stiffness as they are its most rigid component. For this reason we chose to study the flexural behavior of the barb. Qualitative observations have been made regarding this behavior, but there is a surprising lack of quantitative data and detailed analysis of their flexure behavior, the mechanisms used by barbs to avoid being permanently deformed, and the reason for their evolution to an unusual asymmetrical shape. In this paper we answer these questions through experimental procedures and theoretical analysis.

## 2. Materials and methods

### 2.1. Test specimens

Feathers of an adult razor-billed curassow (*Mitu tuberosum*) were obtained postmortem and stored at ambient conditions. Feathers from the left wing within a total length range of 31–34 cm were used in experiments. To prepare the specimens for mechanical testing, barbs were cut from the trailing side of each feather, within the middle section of the rachis (between 45% and 80% of the total feather length). The ends of the barbs (on average approximately 25% of total barb length) were attached to a puck in groups of four. This number was chosen to provide a minimum amount of barbs that would allow for sufficient barbule interlocking. For the single barb tests, surrounding barbs were removed using a scalpel. Initial mounting of the barbs ensured that all had similar orientation, since barbules hold the barbs in place.

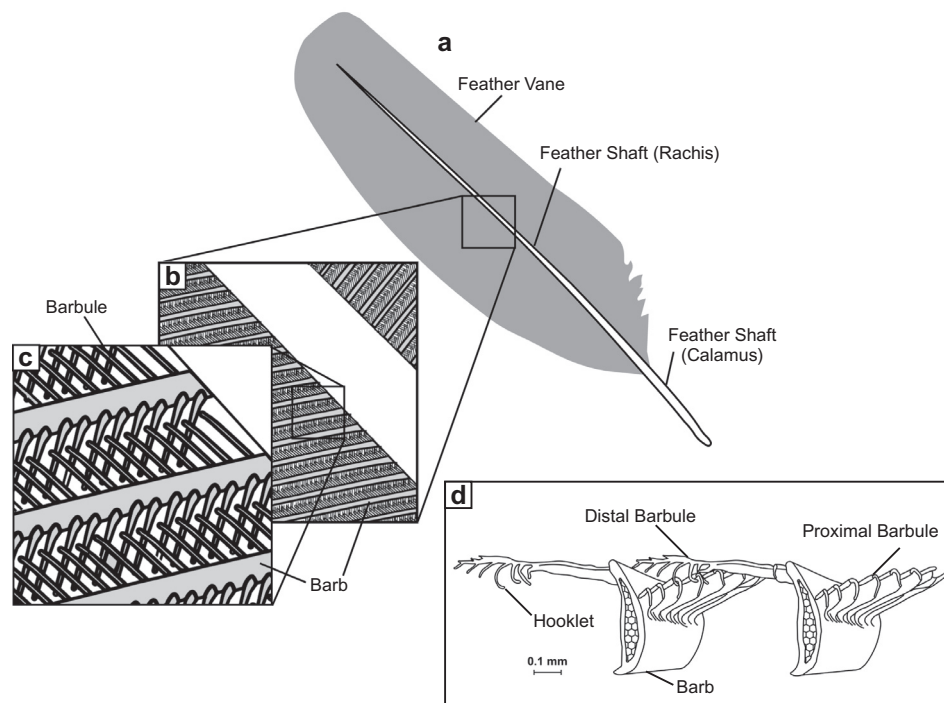


**Fig. 1.** Feather structure: (a) feather shaft (rachis) and the feather vane (barbs and barbules). (b) Barbs branch from the rachis and (c) barbules are minute beams that branch from barbs. (d) Barb and barbule structure: barbs are asymmetrically shaped and foam filled. On the distal side of the barb barbules have hooklets and on the proximal side barbules are grooved. Barbules from neighboring barbs interlock with each other. Inset (d) redrawn after Lucas and Stettenheim (1972) [7].

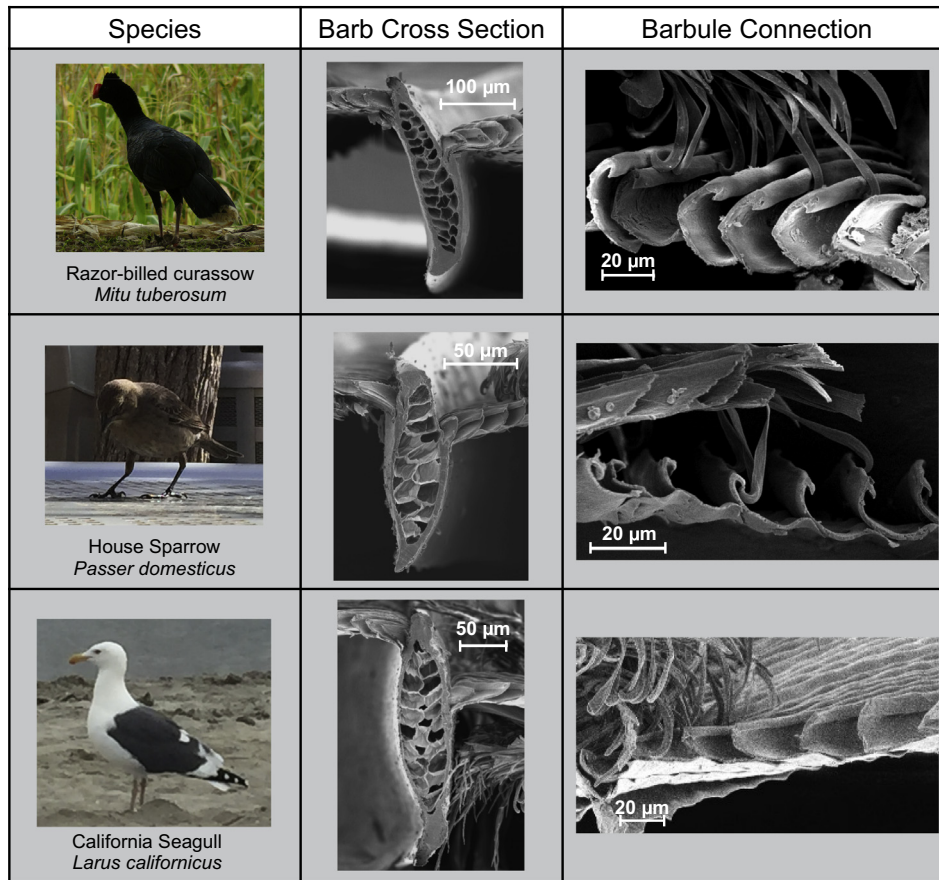


**Fig. 2.** Barbs and barbules from various bird species: in nearly all flying birds, barbs and barbules have a similar shape, as demonstrated in this comparison between the razor-billed curassow (*Mitu tuberosum*), house sparrow (*Passer domesticus*), and California seagull (*Larus californicus*). Razor-billed curassow photograph acknowledgement: Whaldener Endo, [https://commons.wikimedia.org/wiki/File:Mitu\\_tuberosa\\_Whaldener\\_Endo.jpg](https://commons.wikimedia.org/wiki/File:Mitu_tuberosa_Whaldener_Endo.jpg), (cropped image).

## 2.2. Mechanical tests

A Bose Electroforce 3200 testing machine with a 50 g Honeywell load cell (S/N: 1475925, Model: 31) was used for mechanical testing. A manufacturer-machined wedge was attached to the load cell screw and the scale was zeroed before measurements. Pucks were mounted onto a piece of aluminum that was clamped in suspension at the top of the machine. A schematic of the experimental setup is shown in Fig. 3.

The samples were loaded and unloaded at a rate of 0.1 mm/s and displaced  $\pm 4$  mm. The barb was loaded on its ventral side to simulate the direction of applied force on a barb as a bird is landing. Each sample completed four loading and unloading cycles and was stopped at a displacement of  $-4$  mm in the fifth cycle. From these tests, force displacement curves were obtained.

A high-resolution digital camera was secured on a fixed tripod facing the set up. Images were taken prior to loading and used to determine the distance from the barb secured in the puck to the point of contact between the wedge and barb. This distance is called the effective barb length.

## 2.3. Scanning electron microscopy

After the tests, each barb was cut at the effective length as well as at its point of connection to the puck. The barbs were then mounted on a vertical Scanning Electron Microscope (SEM) stub, coated in iridium and imaged using a SEM. Some of the puck images were not used in analysis due to difficulty in obtaining clear images of cross sections after the experiment because of remnants

of the adhesive on samples. We followed a similar procedure to image cross sections of three untested barbs at 10% increments along their length.

## 2.4. Computer aided-design measurements

Since barbs have an asymmetric and tapered structure, to accurately understand our data we characterized the shape change of barbs by measuring their respective area moments of inertia. We found these values for SEM images of barb cross-sections by tracing the barb's foam and cortex using SolidWorks (SolidWorks Corp., Waltham, MA, USA). Since the values given by SolidWorks were for the principal axes of the shape, they were transformed by applying a rotation so that the axes of all measurements were aligned with each other. The angle was calculated with the assumption that the hooked barbules remain horizontal along the length of the barb. While the area moments of inertia found using SolidWorks are with respect to the centroid of the foam or cortex, and not with respect to the total structure's neutral axis (which could not be found using SolidWorks), they are an accurate estimation.

## 2.5. Finite element modeling

The geometry of a sample's cross-section at its connection to the puck and at the end of its effective length was replicated from SEM images. In order to take into account the angular twisting of the barb, we assumed that the hooked barbules remain horizontal throughout the barb. We then executed a sweep between the two

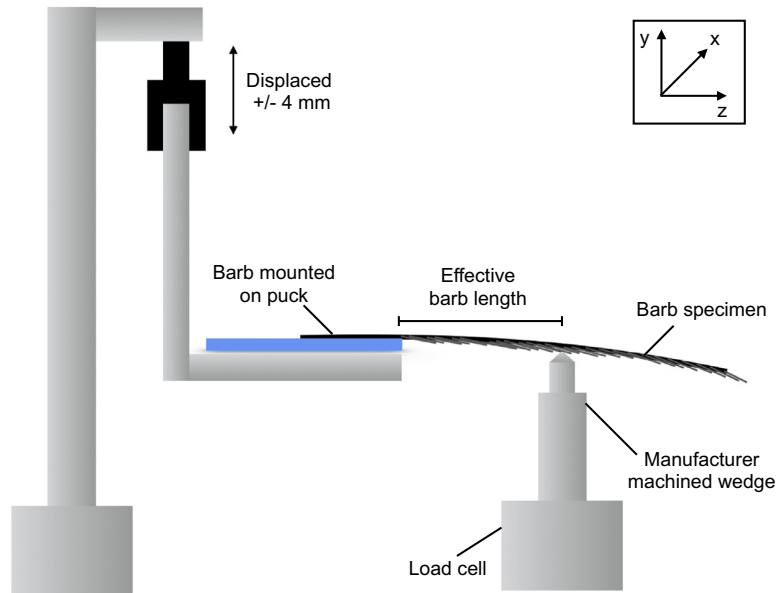


Fig. 3. Experimental configuration: cantilever flexure tests on single barbs and four zipped barbs.

cross sections along the effective length to replicate the tapered structure of our experimental sample. Constituents of the cross section were considered isotropic and homogeneous, and included the cellular core  $E_{\text{foam}} = 0.36$  GPa,  $\nu_{\text{foam}} = 0.33$  and the cortex  $E_{\text{cortex}} = 5.50$  GPa,  $\nu_{\text{cortex}} = 0.40$ , as explained in Section 3.1.

### 2.6. Statistical analysis

In order to minimize any localized noise spikes, raw data sets were smoothed with a median filter incorporating five surrounding points using the software Origin 9.0 (OriginLab Corp, Northampton, USA). This software was also used to find the standard error of the linear fit to the data's slope, which is included as error bars in Figs. 8 and 9. This error was translated into a percent and used to obtain a displacement error, which is accounted for as error bars in Fig. 12.

## 3. Theory and calculations

### 3.1. Elastic modulus of the barb's foam-filled center

To create a theoretical model of the deflection behavior of a barb, one first has to determine the elastic modulus of its foam-filled core. This was calculated using the Gibson and Ashby [13] equations. The foam cells inside the barb were modeled as close-celled hexagonal prisms. From geometrical measurements of SEM images, the relative core/shell density ratio was found to be 0.152. This value, along with other geometrical parameters, was used to find the foam's relative elastic modulus:

$$\frac{E^*}{E_s} \approx \phi^2 \left( \frac{\rho^*}{\rho_s} \right)^2 + (1 - \phi) \frac{\rho^*}{\rho_s}. \quad (1)$$

The gas pressure component of the equation was omitted because of the porous cell wall structure observed in SEM images. The variables are defined such that  $E^*$  is the elastic modulus of the foam,  $E_s$  is the elastic modulus of the solid cortex,  $\phi$  is the volume fraction of the solid contained in the foam's cell edges,  $\rho^*$  is the density of the foam, and  $\rho_s$  is the density of the solid cortex [13]. The full calculations can be found in Appendix A.

By assuming that the elastic modulus of the barb cortex is equal to that of the rachis cortex, and using the accepted value of 5.50 GPa from literature for two-point bending [14], the elastic modulus of the foam core was calculated to be 0.36 GPa. The Poisson's ratio  $\nu_{\text{cortex}} = 0.40$  matched the value used by Bachmann et al. [14] for the rachis, where the value for a similar keratinous material is used because it has not been determined for feather keratin. Similarly, the Poisson's ratio of barb foam is unknown and therefore it was taken to be 0.33, which is the average value for closed cell foam according to Gibson and Ashby [13].

### 3.2. Simplified block model of single barb deflection

A simplified model of the barb's complex geometry was created using rectangular blocks to form an asymmetrical cortex with a constant cross section and a foam-filled interior. The dimensions of the model were iterated until the x- and xy-area moments of inertia of the cortex and the x-area moment of inertia of the foam matched their respective counterparts found for the equivalent experimental barb (as discussed in Section 4.3.1). These were deemed to be the most significant area moments of inertia to match our model due to their contributions in the cantilever flexure equation given in Section 3.2.2. The length of the barb was set to equal 7.8 mm to match the length of the experimental barb.

#### 3.2.1. Finding the location of the neutral axis

Due to significant contributions in bending from the sidewalls, the barb structure could not be simplified using the volume fraction composite method. Additionally, because the barb is an asymmetric structure, the neutral axis does not pass through the centroid. The barb's neutral axis was calculated first.

The derivation begins with the assumption that plane cross-sections remain plane, so that strain is a linear function of x and y (Eq. (2)), and therefore by Hooke's law stress is as well (Eq. (3)) [15]. Definitions of variables are presented in Table 1.

$$\varepsilon_z^{(i)} = ax + by; \quad \sigma_z^{(i)} = E_i(ax + by). \quad (2, 3)$$

**Table 1**  
Definitions of variables used in Eqs. (2)–(18).

Symbol	Definition
$a$	Curvature of barb in the x-direction
$b$	Curvature of barb in the y-direction
$\epsilon_z^{(i)}$	Strain (z-axis) of each component i
$\sigma_z^{(i)}$	Stress (z-axis) of each component i
$E_i$	Elastic modulus of each component i
$x_{ci}$	Location of centroid of each component (along x)
$y_{ci}$	Location of centroid of each component (along y)
$A_i$	Area of each component
$M_x$	Moment in the x-direction
$M_y$	Moment in the y-direction
$I_{xy}^i$	The product of inertia of component i with respect to the x and y axes
$I_x^i$	The x-moment of inertia of component i
$I_y^i$	The y-moment of inertia of component i
$\theta$	The angle between the location of the applied load and the y-axis

After these assumptions are made, the sum of the integrated stress of each component is set to equal zero to determine the location of the neutral axis (Eq. (4)):

$$\sum_{i=1}^n \int_{A_i} \sigma_z^{(i)} dA = 0. \quad (4)$$

The linear stress condition is applied:

$$\sum_{i=1}^n E_i \int_{A_i} (ax + by) dA = 0. \quad (5)$$

The elastic modulus of each component is taken into account in contributing to the location of the neutral axis:

$$\sum_{i=1}^n E_i [ax_{ci} A_i + by_{ci} A_i] = 0, \quad (6)$$

$$a \sum_{i=1}^n E_i A_i x_{ci} + b \sum_{i=1}^n E_i A_i y_{ci} = 0. \quad (7)$$

The location of the neutral axis ( $x_0, y_0$ ) is solved using:

$$\sum_{i=1}^n E_i A_i (x_{ci} - x_0) = 0, \quad \sum_{i=1}^n E_i A_i (y_{ci} - y_0) = 0. \quad (8, 9)$$

The solutions for the specific case of the barb are found in [Appendix B](#).

### 3.2.2. Deriving the inverse curvature and deflection of the barb in flexure

The curvature is derived in order to solve for the barb's deflection. The relationship between the moment  $M_x$  and the stress in each component (Eq. (10)) was used to find the relationship between the curvatures  $a$  and  $b$ :

$$M_x = \sum_{i=1}^n \int_{A_i} y \sigma_z^{(i)} dA. \quad (10)$$

Since the moments are known, the equations can be solved for numerical values. A similar process for  $M_y$  is applied and shown in [Appendix C](#). The linear stress condition was applied to yield Eq. (11), and then these values were integrated (Eq. (12)).

$$M_x = \sum_{i=1}^n \int_{A_i} y E_i (ax + by) dA, \quad (11)$$

$$M_x = \sum_{i=1}^n E_i \left[ a \int_{A_i} xy dA + b \int_{A_i} y^2 dA \right]. \quad (12)$$

These equations are further simplified to include area moments of inertia:

$$M_x = \sum_{i=1}^n E_i [a I_{xy}^i + b I_x^i], \quad (13)$$

$$M_y = a \sum_{i=1}^n E_i I_{xy}^i + b \sum_{i=1}^n E_i I_x^i. \quad (14)$$

The following variables were then introduced to simplify the calculations of solving for  $a$  and  $b$ :

$$E = \frac{\sum_i E_i A_i}{A}, \quad I_x = \frac{\sum_i E_i I_x^i}{E}, \quad I_y = \frac{\sum_i E_i I_y^i}{E}, \quad I_{xy} = \frac{\sum_i E_i I_{xy}^i}{E}.$$

Using these variables, the moment equations are rewritten as:

$$M_x = a E I_{xy} + b E I_x; \quad (15)$$

$$-M_y = a E I_y + b E I_{xy}. \quad (16)$$

Upon solving Eqs. (15) and (16) for  $a$  and  $b$ , we obtain Eqs. (17) and (18), which also specify the relationship between the curvatures  $a$  and  $b$  and deflections  $u$  and  $v$  [16].

$$a = \frac{I_{xy} M_x + I_x M_y}{E(I_{xy}^2 - I_x I_y)} = -\frac{\partial^2 u}{\partial z^2}, \quad (17)$$

$$b = -\frac{I_y M_x + I_{xy} M_y}{E(I_{xy}^2 - I_x I_y)} = -\frac{\partial^2 v}{\partial z^2}. \quad (18)$$

The differential Eqs. (17) and (18) are solved to produce Eqs. (19) and (20) which describe deflections in the x( $u$ ) and y( $v$ ) directions.

$$u = \frac{I_{xy} F_y z^3}{3E(I_{xy}^2 - I_x I_y)}, \quad (19)$$

$$v = -\frac{I_y F_y z^3}{3E(I_{xy}^2 - I_x I_y)}. \quad (20)$$

A sketch of the simplified barb used in calculations is shown in [Fig. A.1](#) along with the definitions of variables used for length are given. Dimensions used are listed in [Table A.2](#) of the [Appendix B](#).

### 3.3. Analytical model of single barb deflection

To more accurately represent the cross sectional changes that occur throughout the barb's effective length, we created a more complex analytical model. We begin with an equation similar to the one described in the previous section:

$$b = -\frac{\partial^2 v}{\partial z^2} = -\frac{M_x I_y(z)}{E_s (I_x(z) I_y(z) - I_{xy}(z))} = \frac{F(L-z) I_y(z)}{E_s (I_x(z) I_y(z) - I_{xy}(z))}. \quad (21)$$

Note that the expression of  $b$  differs from Eq. (18):  $E_s$  is the cortex's elastic modulus, the load is only considered in the y-direction,  $L$  refers to the effective length, and  $I_x(z)$ ,  $I_y(z)$  and  $I_{xy}(z)$  are equivalent inertias of the geometry. These inertias follow a z-dependent trend that takes into account the cross-sectional changes. As stated in Sections 2.3 and 2.4, we characterized this trend by measuring the  $I_x$ ,  $I_y$ , and  $I_{xy}$  of three different barbs at every 10% along their length. Moreover, we defined  $I_x$ ,  $I_y$ ,  $I_{xy}$  such that:  $I_x = I_{xcortex} + \alpha I_{xfoam}$ ,  $I_y = I_{ycortex} + \alpha I_{yfoam}$ ,  $I_{xy} = I_{xycortex} + \alpha I_{xyfoam}$  where  $\alpha$  is a weighing factor that takes into account the fact that the foam has differing elastic properties ( $\alpha = \frac{E_f}{E_s}$ , see Eq. (1) and [Appendix A](#) for details).

From Eq. (21) we integrate twice to find the deflection  $v$  at the end of the cantilever, with the imposed boundary conditions  $v = 0$  and  $dv/dz = 0$  at  $z = 0$ :

$$\frac{\partial v}{\partial z} = \frac{F}{E_s} \int_0^z \frac{I_y(z)(L-z)}{I_x(z)I_y(z) - I_{xy}^2(z)} dz, \quad (22)$$

$$v(L) = \frac{F}{E_s} \int_0^L dz \int_0^z \frac{I_y(\zeta)(L-\zeta)}{I_x(\zeta)I_y(\zeta) - I_{xy}^2(\zeta)} d\zeta. \quad (23)$$

#### 3.4. Finite element model of a single barb in flexure

The finite element model (FEM) mimicked the conditions of the aforementioned experiment. The barb was lowered by a given vertical displacement. The end of the barb was fixed while the tip contacted an analytically rigid cylindrical wedge. A hard contact interaction was defined between the two solids, and the reaction force was measured at the wedge.

### 4. Results and discussion

#### 4.1. Materials characterization

The cross sections of untested feather barbs show that closer to the rachis the barb is highly asymmetric; it becomes smaller and more symmetrical towards the tip (Fig. 4a), as previously observed by Proctor et al. [6]. Foam core cells were found to be most homogeneous in size at the tip and most diverse in size between the rachis and the center of the barb (Fig. 4b–d). Perhaps a larger total

area of foam allows nature to create cells of varying size, with larger cells at the interior of the barb to reduce the amount of material and decrease density while maintaining bending resistance. Indeed, this has been observed in the porcupine quills, which consist of a keratinous foam-filled shell [17,18].

Along the barb the cortex area to foam core area ratio ranges from 0.7 to 2.3. The ratio slightly decreases from 10 to 20 percent of the barb's length, and then increases from 40 to 70 percent. Towards the end of the tip the relative amount of cortex increases to compensate for the smaller cross sectional area. It is plausible that this range of ratios is optimized for the stiffness, weight and type of loading the barb experiences in flight.

Throughout its length, the barb's dorsal-ventral stiffness is reinforced by dorsal-ventral cortex walls which are thicker than the lateral cortex walls. This is for two reasons: (1) higher loading in flight is applied to the barb in the dorsal-ventral direction, and (2) the barb is able to twist along its lateral walls when loading becomes critically large. The  $x$ -,  $y$ - and  $xy$ -area moments of inertia of the barb's cortex and foam were found to follow an exponential decay trend, as shown in Fig. 5.

#### 4.2. Cyclic testing of single barbs

A representative experimental plot of displacement and force versus time displayed in Fig. 6 shows that the resistance force initially rises linearly with an increase in displacement, and then slightly decreases as the barb twists. Twisting along the  $z$ -axis causes the stiffness to decrease with respect to the  $y$ -axis because its height is now its width. Since this twisting occurs before the

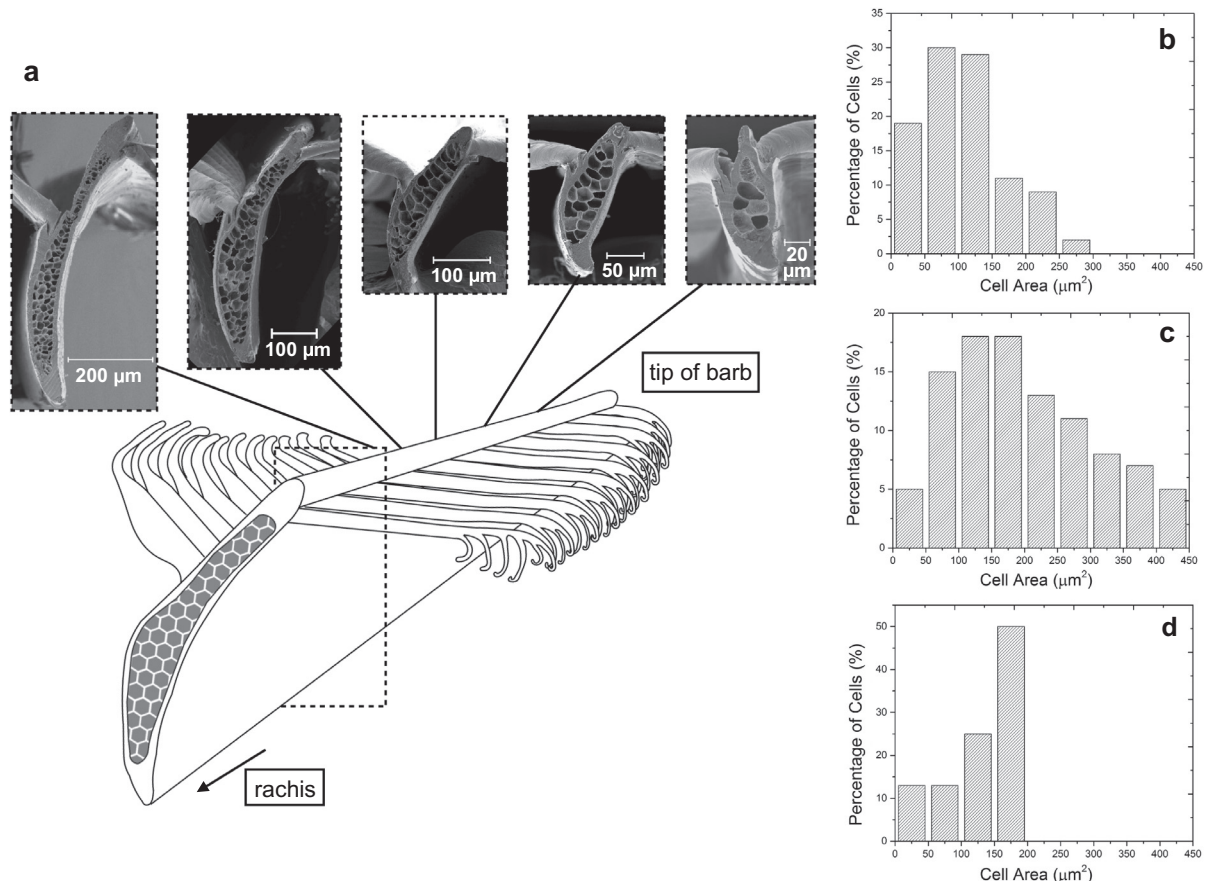


**Fig. 4.** (a) Barb cross sectional shape and size: the barb becomes smaller and more symmetrical towards the tip. Characterizing the foam of the barb: The cell size distribution of the foam shows that at (b) 5% and especially (c) 30% from the rachis the cell size is more diverse than at (d) 90% of the barb length from the rachis.

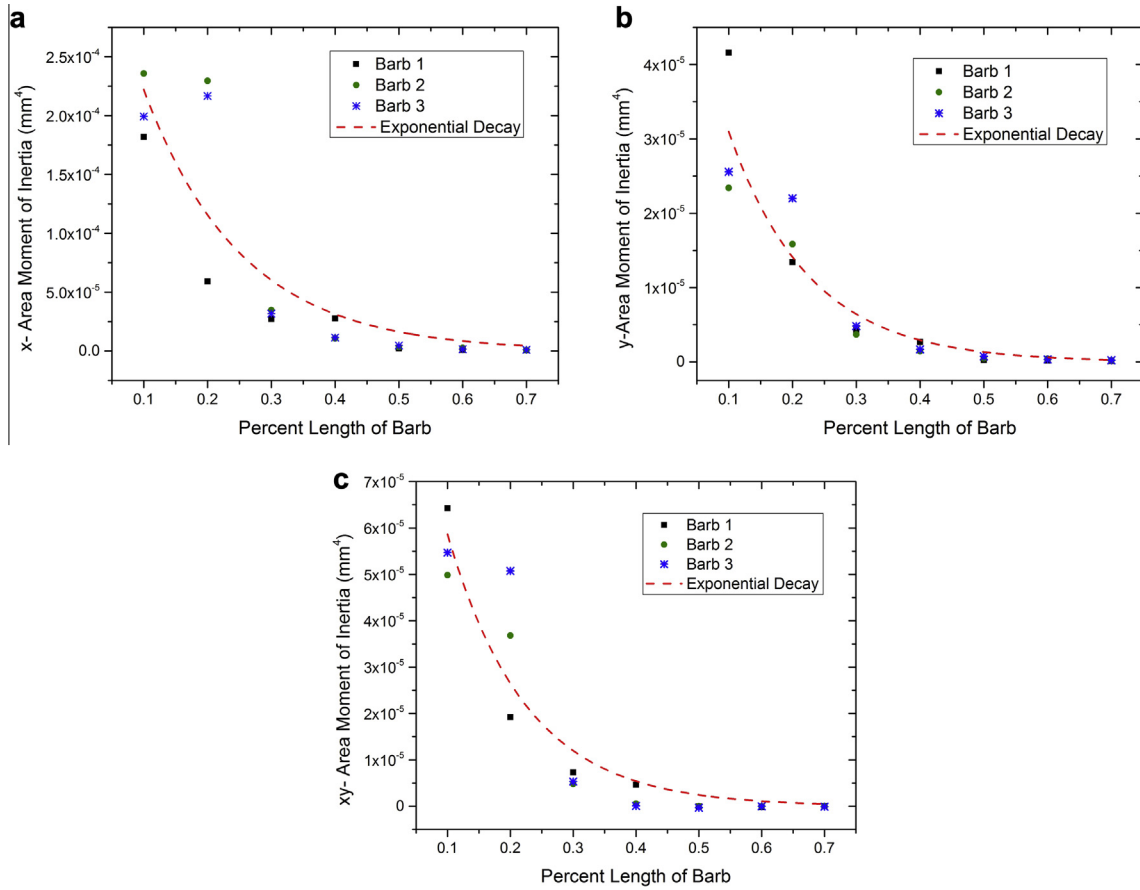


**Fig. 5.** The (a) x-, (b) y- and (c) xy-area moments of inertia of the barb's cortex and foam were found to follow an exponential decay trend. The foam and cortex were combined as explained in Section 3.3.

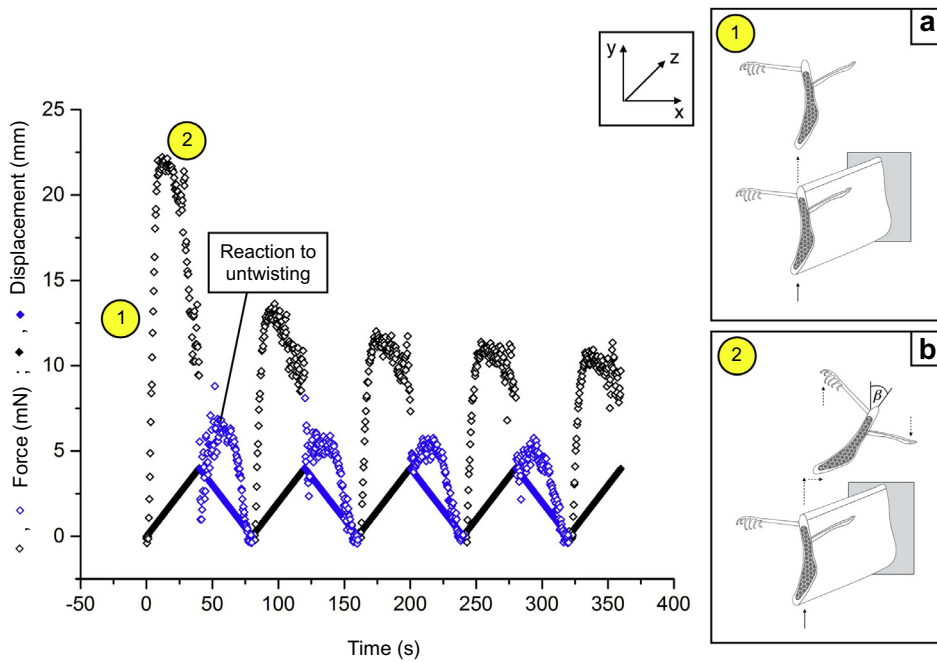


**Fig. 6.** The deflection of a barb: a typical experimental plot of displacement and force as a function of time. Black indicates loading and blue indicates unloading. The barb first (a) deflects in the y-direction, then (b) twists, resulting in a decrease in stiffness with respect to the y-axis.

maximum displacement, the maximum resistive force appears just before the barb twists, not at the point of maximum displacement. The insets (a) and (b) of Fig. 6 explain this process of barb flexure. When the barb is unloaded, the resistive force sharply drops and then rises as a reaction to the untwisting of the barb. This trend is apparent for each of the four cycles of all tests. Through this flexure stratagem, the barb can undergo large displacements without catastrophic failure. These results are similar to visual observations by Butler et al. [19], who stated that the asymmetry, thinner lateral walls of the cortex, and slenderness of the barb result in its twisting when dangerously large loads are applied. It is important for the barbs to deform without mechanically failing because they are essential to bird flight and are only replaced during molting, which usually occurs annually [20]. This twisting action also ensures that loads are distributed more effectively to neighboring barbs.

To understand the repeatability of the flexure tests, the maximum force of the first and second cycle were compared. The difference between these forces, measured in percentage (which we define as percent damage), is plotted versus the maximum force and effective barb length (Fig. 7). Shorter barbs require higher forces for damage and have a larger percent damage that likely corresponds to yielding, including linear and permanent deformation of the cortex. Longer barbs have lower maximum forces and a smaller percent damage which conceivably corresponds to elastic instability (buckling). Examples of experimental force versus deflection plots for two test cycles are shown in the inset of Fig. 7, one with (a) 40% and another with (b) 7% damage. Although some of the tests show significant amounts of damage, the barbs continue to offer some level of resistance and it has been reported (Liu et al. [21]) that this damage can be reversed by hydration.

#### 4.3. Linear deflection of single barbs

The slope of the linear portion of the first cycle of force versus deflection curves for experimental trials was plotted against the effective length of the samples in Fig. 8. As expected by the classic cantilever equation,  $Force/Deflection = (3 * EI)/Length^3$ , the force/

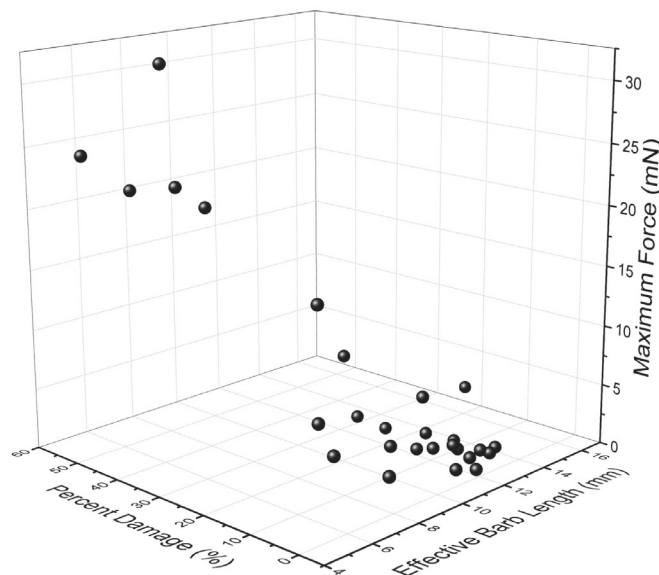


**Fig. 7.** The repeatability of flexure tests: the maximum force and effective barb length are plotted against the percent damage between the first and second cycles. With shorter barbs there are higher resistive forces and stresses, therefore the percent damage increases. The insets show examples of force displacement curves for two cycles of loading and unloading of single barbs with (a) 40% (b) 7% damage.

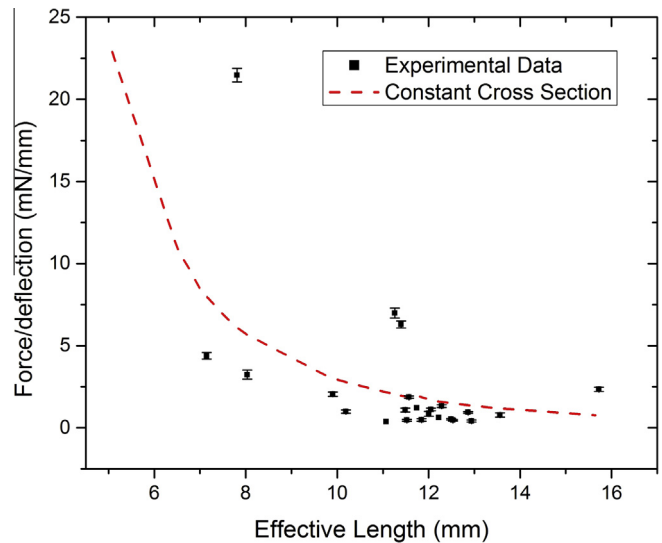
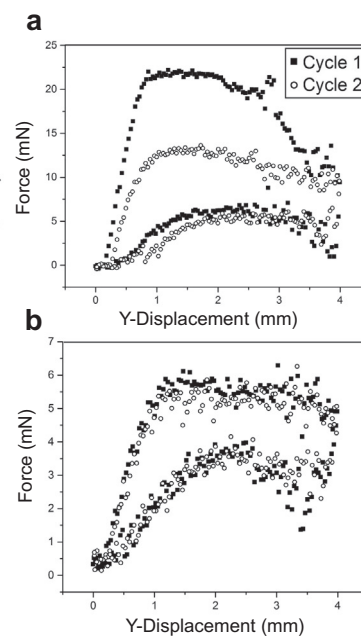


**Fig. 8.** Experimental slope of force versus deflection: the slope of the linear portion of the first cycle of experimental trials versus the effective length of each sample. The slope of a barb with a constant cross section throughout its length is shown for comparison.

deflection increases with a reduction in effective length. The average of the moments of inertia for the SEM images of the barb at the point of connection to the puck were taken and assumed to be a constant cross section for comparison to experimental data. Since the barbs are a tapered cross section with some variation in size, there is slight deviation from this trend.

#### 4.3.1. Comparison between the experimental results and models

Since we observed a rapid decay for the values of area moments of inertia along the length of the barb, we were able to predict equivalent moments of inertia for all samples for which we had clear puck and effective length end images. We assumed an exponential decay correlation between the area moments of inertia of



these two sections and integrated between the percentages of barb length to find an equivalent area moment of inertia representing the tapered structure. By injecting these values of moments of inertia into Eq. (22), we were able to calculate an analytical force/deflection for experimental data. This is plotted with the experimental data as a histogram in Fig. 9.

Images of the FEM simulation with the von Mises stresses plotted are shown in Fig. 10. Near the side of the barb held in place, stresses are highest on the dorsal and ventral sides. Perhaps this further explains why cortex walls are thicker on those sides. At the point at which the barb contacts the wedge, stresses are highest on the ventral side at the foam-cortex interface due to compression. These high stresses could indicate the location of the first point of failure.

The simplified block model, analytical model, and FEM are compared with a sample's experimental data in Fig. 11. As demonstrated in this figure, all models are in reasonable agreement with the data. The FEM simulations provide a method of justifying the experimental results by accounting for the complicated geometry and simulating experimental conditions to great detail. The analytical model allows us to compare our theory with multiple experimental data points with relative ease. Lastly, the simplified block model enables an improved understanding of the deflection and explains the structural response of barb deformation so that it might be applied to engineered synthetic structures.

4.4. Deflection of multiple barbs

The linear region of the force-deflection curve describes flexure before the yielding of the structure. Experiments reveal that this region extends to a larger displacement for groups of four zipped barbs compared to single barb samples. The highlighted region of Fig. 12a, b is the linear portion of four zipped barbs and single barb flexure test cycles, respectively. The arrowed line in each plot represents the y-displacement corresponding to the linear region, which we define as *r*. This value of *r* is plotted in Fig. 12c against the effective barb length for four zipped barbs and single barb tests.

Four zipped barbs are made more robust by the adhesion of the barbules to one another. This adhesion postpones the onset of barb

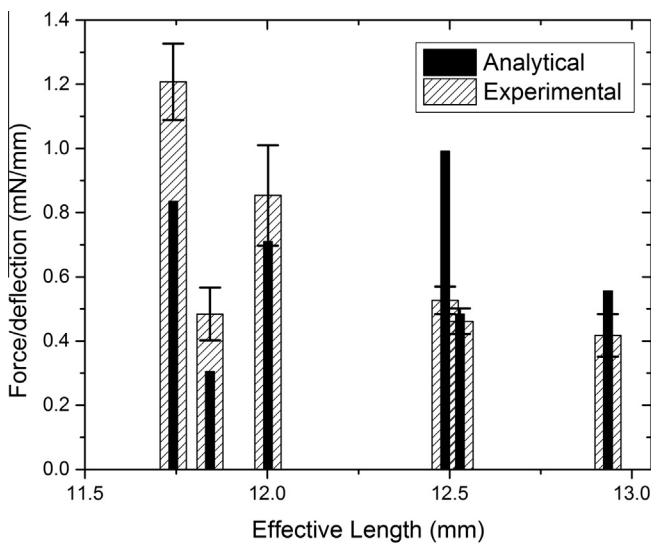


Fig. 9. Comparison between the analytical and experimental force/deflection for the linear region of single barbs. Analytical calculations are based on the method described in Section 3.3.

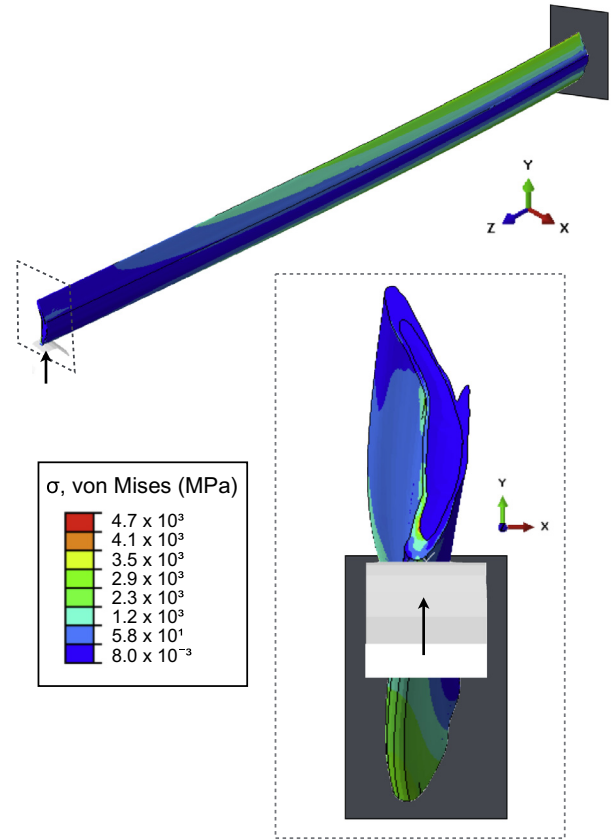


Fig. 10. Finite element model of the deflected barb with the von Mises stress (MPa) plotted. Higher stresses appear on the dorsal and ventral sides of the end held in place and at the foam-cortex interface of the end contacting the wedge.

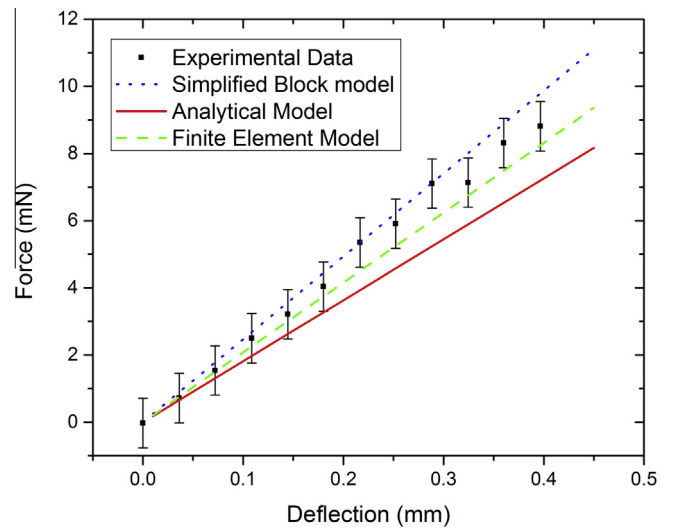
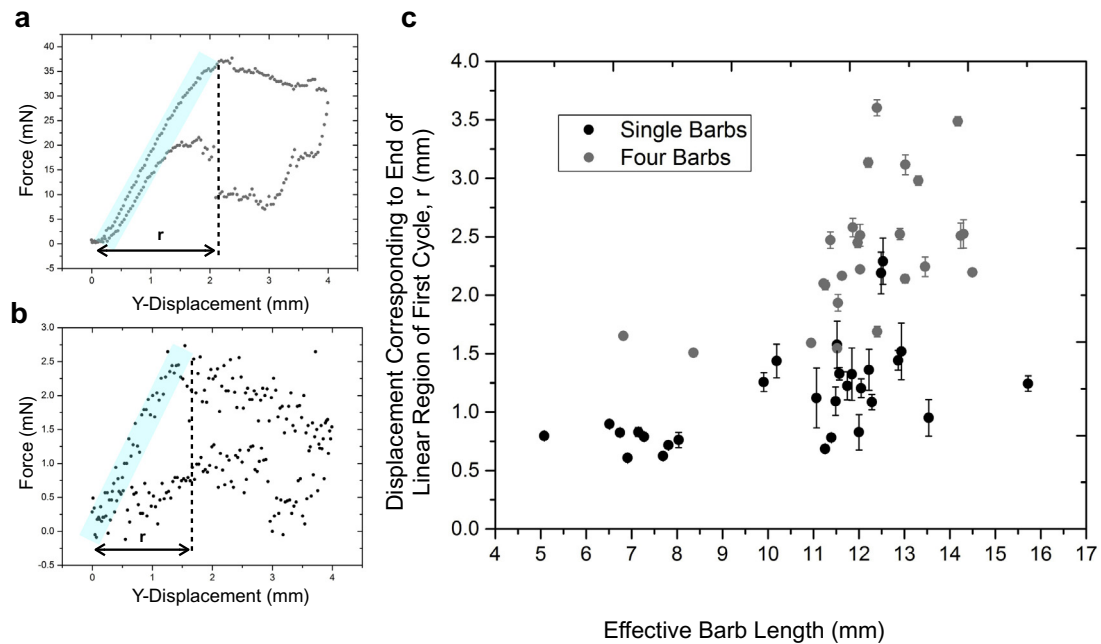


Fig. 11. Comparison of the force versus deflection of an experimental run, a representative simplified block model, analytical model, and finite element model.

twisting, thereby preventing the reduction in stiffness with respect to the y-axis, which results in yielding of the structure. This is consistent with visual observations by Butler et al. [19], who stated that there is an increase in lateral stability when groups of barbs are attached to each other. The flexure behavior of the feather vane can therefore be tailored by the adhesive mechanism between barbs, allowing for a system that mitigates damage. For example,



**Fig. 12.** Yielding point of four-zipped barbs and single barbs: an example of the first cycle of flexure tests for (a) four-zipped barbs and (b) single barbs. The linear portion of the cycle to the point of yielding is highlighted. The arrowed line “r” shows the y-displacement corresponding to the end of the linear region. This displacement “r” is plotted against the effective barb length in (c) and indicates that four-zipped barbs are able to deflect to larger amount without yielding than single barbs.

if a part of the feather vane is severely damaged, the total vane will not be compromised because the damaged portion will become detached as critically large loads are applied.

#### 4.5. Strengthening mechanisms of the feather vane

The adhesion mechanism that accounts for progressive deformation of the feather consists of the outward sliding of the barbules in the grooves of the juxtaposed barbs. As stated in the introduction, this mechanism is similar to a “Velcro” connection that allows neighboring barbules to hold (hook) barbs together.

Hooklets on the distal barbules slide along the grooved proximal barbules, allowing barbs to move closer and further from each other. Fig. 13a is a micrograph of the hooklet interlocking with a grooved proximal barbule, and Fig. 13b shows a series of zipped barbule connections. A three-dimensional model inspired by this mechanism and created by three-dimensional printing (additive manufacturing) is shown in Fig. 13c. Multiple hooks slide into each groove and enable the reversible separation of adjacent barbs. Ideas from the feather vane mechanism can inspire new types of single-direction adhesives or lightweight, damage tolerant aerospace materials.

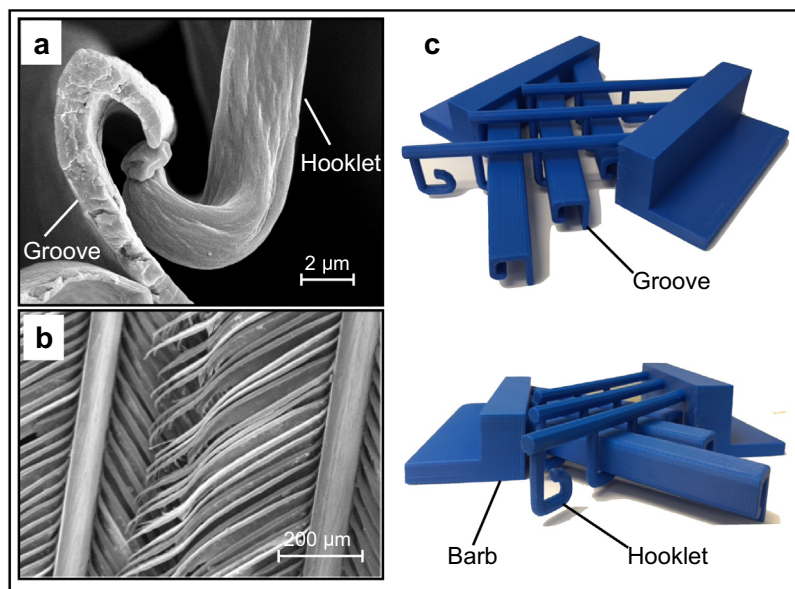


**Fig. 13.** The interlocking structure of the barbules: micrographs of the House sparrow (*Passer domesticus*) show (a) the hooklet sliding into the grooved proximal barbule, (b) overlapping barbules within a feather. This interlocking mechanism was simplified and then constructed using additive manufacturing to create a three-dimensional model (c).

## 5. Conclusions

The morphology of the feather vane was investigated and the flexural behavior of un-zipped and zipped barbs was quantitatively measured for the first time. The following significant enhancements of our understanding were accomplished:

- When loaded in cantilever orientation, un-zipped barbs deflect in the y-direction and then twist due to their asymmetry. By twisting the barb becomes less stiff with respect to its y-axis and therefore its maximum resistive force occurs before the maximum displacement of the barb.
- A finite element simulation, analytical model and a simplified block model were found to accurately describe the linear flexure behavior of a single barb.
- It was established experimentally that compared to un-zipped barbs, zipped barbs displace to a greater distance before yielding due to barbules which prevent barb rotation.
- A barbule-inspired interlocking mechanism is proposed and created through additive manufacturing.
- The insights obtained from this experimental study, along with the theoretical models and FEM, will be useful for creating a variety of bioinspired structures ranging from materials with a tailored stiffness to new adhesives.

## Acknowledgements

This work is supported by the University of California San Diego Materials Science Program and the AFOSR MURI (AFOSR-FA9550-15-1-0009). We would like to thank Andy Kietwong and Kyle Adriany for helpful discussion and Paulina Villegas and David Moncivais for image data gathering.

## Appendix A. Foam calculations

The closed-cell foam inside of the barb was simplified to a hexagonal prism shape. The relative density was calculated where  $A_r$  is the cell's aspect ratio [13]:

$$\frac{\rho^*}{\rho_s} = \frac{2}{\sqrt{3}} \frac{t}{l} \left\{ 1 + \frac{\sqrt{3}}{2A_r} \right\}.$$

Table A.1 shows the definitions and values measured for each variable.

Next, the volume fraction was calculated [13]:

$$\phi = \frac{t_e^2}{t_e^2 + \frac{Z_f}{n} t_f l}.$$

**Table A.1**

Values for foam calculations.

Variable	Definition	Value
$\rho^*/\rho_s$	Density of foam/Density of solid	$0.152 \pm 0.08$
$t = t_f$	Thickness of foam cell-wall	$0.875 \pm 0.37 \mu\text{m}$
$l$	Foam cell edge length	$9.78 \pm 2.37 \mu\text{m}$
$A_r$	Aspect ratio $h/l_f$	$1.83 \pm 0.67$
$h$	Height of foam cell	$17.92 \pm 4.97 \mu\text{m}$
$t_e$	Thickness of foam cell edge (corner)	$3.39 \pm 2.08 \mu\text{m}$
$\phi$	Volume fraction of cell located in the cell edges	$0.627 \pm 0.83$
$Z_f$	Number of faces that meet at an edge on a single cell	$3.6$ [10]
$\bar{n}$	Average number of cells per single cell	$4.5$ [10]
$\frac{E_s}{E_s}$	Foam elastic modulus/Solid material elastic modulus	$0.066$

This is the volume of solid material contained in cell edges. The remaining volume fraction of the cell ( $1 - \phi$ ) is in cell faces.

Lastly, to find the relative elastic modulus we used [13]:

$$\frac{E^*}{E_s} \approx \phi^2 \left( \frac{\rho^*}{\rho_s} \right)^2 + (1 - \phi) \frac{\rho^*}{\rho_s},$$

where the influence from internal gas pressure is ignored because of the porosity observed in SEM images of the cells.

Using the value from literature for the cortex of the rachis [14], the elastic modulus of the solid cortex ( $E_s$ ) of the barb is taken to be 5.50 GPa.

## Appendix B. Determining the location of the neutral axis

Using the dimensions given in Fig. A.1, the location of the neutral axis for each rectangular piece is solved for in terms of an arbitrarily set location of the overall neutral axis ( $x_0, y_0$ ), which incorporates the elastic modulus of each piece:

The location of the centroid of each rectangular piece ( $x_{ci}$ ) is determined along the x-axis:

$$x_1 = -h_3 + x_0 + \frac{\delta_1}{2},$$

$$x_2 = -h_3 + x_0 + \delta_5 + \frac{\delta_2}{2},$$

$$x_3 = -h_3 + x_0 + \frac{h_3}{2},$$

$$x_4 = x_0 - h_3 + \delta_2 + \delta_5 + \frac{\delta_4}{2},$$

$$x_5 = -h_3 + x_0 + \frac{\delta_5}{2}.$$

The location of the centroid of each rectangular piece ( $y_{ci}$ ) is determined along the y-axis:

$$y_1 = -h_2 + y_0 - \frac{h_1}{2},$$

$$y_2 = -\frac{h_2}{2} + y_0,$$

$$y_3 = y_0 + \frac{\delta_3}{2},$$

$$y_4 = -\frac{h_4}{2} + y_0,$$

$$y_5 = -\frac{h_5}{2} + y_0.$$

These equations are used in the Eqs. (8) and (9) to find the actual location of the neutral axis  $x_0, y_0$ .

$$x_0 = h_3 - \frac{E_1[\delta_1 A_1 + h_3 A_3 + A_4(2\delta_2 + \delta_4 + 2\delta_5) - \delta_5 A_5] + E_2(\delta_2 A_2 + 2\delta_5 A_2)}{2[E_1(A_1 + A_3 + A_4 + A_5) + E_2 A_2]},$$

$$y_0 = \frac{E_1(2h_2 A_1 + h_1 A_1 - \delta_3 A_3 + h_4 A_4 + h_5 A_5) + E_2(h_2 A_2)}{2[E_1(A_1 + A_3 + A_4 + A_5) + E_2 A_2]}.$$

The specific values used in calculations can be found in Table A.2.

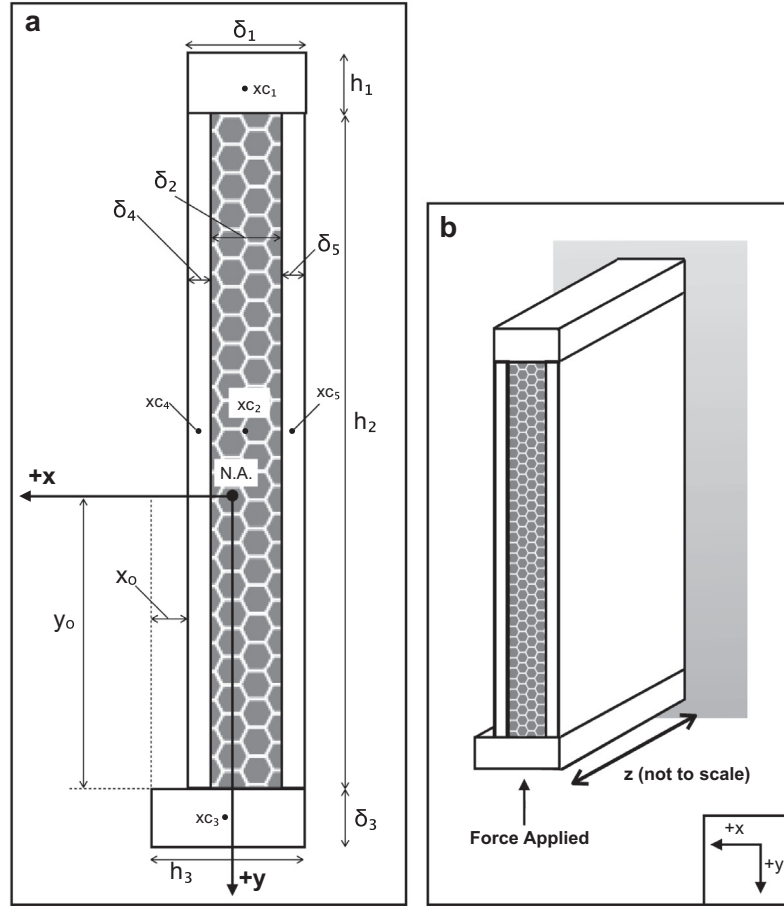


**Fig. A.1.** Simplified barb used in theoretical calculations: (a) the definitions of dimensions used, where  $h_2 = h_4 = h_5$  (b) sketch of the orientation of the applied force.

**Table A.2**  
Simplified barb dimensions. Units are in micrometers unless otherwise labeled.

Dimension	
$\delta_1$	79
$\delta_2$	48
$\delta_3$	39
$\delta_4$	16.5
$\delta_5$	16.5
$h_1$	40
$h_2$	454
$h_3$	103
$h_4$	454
$h_5$	454
$z$	7809
$I_{xcortex}$	$6.93 \times 10^8 \mu\text{m}^4$
$I_{xfoam}$	$3.76 \times 10^8 \mu\text{m}^4$
$I_{xycortex}$	$1.14 \times 10^7 \mu\text{m}^4$

### Appendix C. Deriving the inverse curvature of $M_y$

The derivation of the relationship between the moment  $M_y$  and the inverse curvature is listed below. This was used to obtain Eqs. (16) and (18) of the main text.

We begin with the moment-stress relationship:

$$M_y = \sum_{i=1}^n \int_{A_i} x \sigma_z^{(i)} dA.$$

By substituting expressions of  $\sigma_z^{(i)}$ , we obtain:

$$M_y = \sum_{i=1}^n \int_{A_i} x E_i (ax + by) dA,$$

i.e.,

$$M_y = \sum_{i=1}^n E_i \left[ a \int_{A_i} x^2 dA + b \int_{A_i} xy dA \right].$$

Therefore:

$$-M_y = a \sum_{i=1}^n E_i I_y^i + b \sum_{i=1}^n E_i I_{xy}^i,$$

where

$$I_y^i = \int_{A_i} x^2 dA \text{ and } I_{xy}^i = \int_{A_i} xy dA.$$

### References

- [1] J. Clarke, Feathers before flight, *Science* 340 (2013) 690–692.
- [2] X. Xu, K. Wang, K. Zhang, Q. Ma, L. Xing, C. Sullivan, et al., A gigantic feathered dinosaur from the Lower Cretaceous of China, *Nature* 484 (2012) 92–95.
- [3] P. Chen, Z. Dong, S. Zhen, An exceptionally well-preserved theropod dinosaur from the Yixian formation of China, *Nature* 391 (1998) 147–152.
- [4] P.R. Stettenheim, The integumentary morphology of modern birds—An overview, *Am. Zool.* 40 (2000) 461–477.
- [5] T. Lingham-Soliar, R.H.C. Bonser, J. Wesley-Smith, Selective biodegradation of keratin matrix in feather rachis reveals classic bioengineering, *Proc. Biol. Sci.* 277 (2010) 1161–1168.
- [6] N.S. Proctor, P.J. Lynch, *Manual of Ornithology: Avian Structure & Function*, first ed., Yale UP, New Haven, 1993.
- [7] A.M. Lucas, P.R. Stettenheim, Structure of feathers, in: *Avian Anat. Integument*, US Department of Agriculture, Washington D.C., 1972, pp. 341–419.
- [8] A. Kovalev, A.E. Filippov, S.N. Gorb, Unzipping bird feathers, *J. R. Soc. Interface* 11 (2014) 20130988.
- [9] J. Barlee, Flight, in: A. Landsborough Thomson (Ed.), *A New Dict. Birds*, Nelson, London, 1964.

- [10] R.H.J. Brown, Flight, in: A.J. Marshall (Ed.), *Biol. Comp. Physiol. Anim.*, Academic Press, New York, 1961.
- [11] L. Alibardi, Cell organization of barb ridges in regenerating feathers of the quail: Implications of the elongation of barb ridges for the evolution and diversification of feathers, *Acta Zool.* 88 (2007) 101–117.
- [12] J.J. Videler, Avian flight, in: T.R. Birkhead (Ed.), *Oxford Ornithol. Ser.*, Oxford University Press, Oxford, 2005.
- [13] L.J. Gibson, M.F. Ashby, *Cellular Solids: Structure & Properties*, second ed., Cambridge University Press, Cambridge, 1997.
- [14] T. Bachmann, J. Emmerlich, W. Baumgartner, J.M. Schneider, H. Wagner, Flexural stiffness of feather shafts: geometry rules over material properties, *J. Exp. Biol.* 215 (2012) 405–415.
- [15] R.D. Cook, W.C. Young, *Advanced Mechanics of Materials*, first ed., Macmillan, New York, 1985.
- [16] E.P. Popov, *Engineering Mechanics of Solids*, second ed., Prentice Hall, Upper Saddle River, 1998.
- [17] W. Yang, J. McKittrick, Separating the influence of the cortex and foam on the mechanical properties of porcupine quills, *Acta Biomater.* 9 (2013) 9065–9074.
- [18] W. Yang, C. Chao, J. McKittrick, Axial compression of a hollow cylinder filled with foam: a study of porcupine quills, *Acta Biomater.* 9 (2013) 5297–5304.
- [19] M. Butler, A.S. Johnson, Are melanized feather barbs stronger?, *J. Exp. Biol.* 207 (2004) 285–293.
- [20] F.B. Gill, *Ornithology*, second ed., W.H. Freeman, New York, 1995.
- [21] Z.Q. Liu, D. Jiao, Z.F. Zhang, Remarkable shape memory effect of a natural biopolymer in aqueous environment, *Biomaterials* 65 (2015) 13–21.